Robotic Patch Clamp Based on Noninvasive 3-D Cell Morphology Measurement for Higher Success Rate

Qili Zhao, *Member, IEEE*, Jinyu Qiu, *Graduate Student Member, IEEE*, Yu Han, Yiqing Jia, Yue Du, *Member, IEEE*, Huiying Gong, Minghui Li, Ruimin Li, Mingzhu Sun, *Member, IEEE*, and Xin Zhao, *Member, IEEE*

***Abstract*— The formation of the gigaseal, a giga Omega-scale seal between the micropipette electrode and cell surface, is the keystone to measure the extremely weak electric signals of cell ion channels in patch clamp technique. To determine a point on the cell surface facilitating gigaseal formation, 3-D cell morphology information is required. However, the current 3-D cell morphology measurement methods relying on special devices or easily causing clogging issues of the micropipette electrode due to contact on cells are usually not applicable in the traditional patch clamp system. Addressing this, a noninvasive 3-D cell morphology measurement method was developed in this article for robotic patch clamp with a higher success rate of gigaseal formation. First, the measured bath impedance of the micropipette electrode was modeled and then utilized to measure the cell surface height noninvasively. Using the measured cell surface heights at key positions, the 3-D cell morphology was fitted to determine a contact position on the cell surface to facilitate gigaseal formation. Finally, a robotic whole-patch clamp process was conducted at the determined contact position. Experimental results demonstrated that 100% and 90% success rates of noninvasive 3-D cell morphology measurements were achieved on the cultured human embryonic kindey (HEK)-293 cells and pyramidal neurons in mouse brain slices, respectively, with an average measurement error of cell surface height less than 0.15 μm. At the determined contact position, significant improvements in success rates of gigaseal formation and whole-cell patch clamp operation were achieved in comparison to the results at the positions recommended in related work. Our research may spike inspiration to improve the success rates of gigaseal formation and patch clamp operation based on 3-D cell morphologies.**

***Index Terms*— 3-D cell morphology measurement, automated cell measurement, microoperation system, robotic patch clamp.**

I. Introduction

DUE to its capability to detect the electric signals of the cell ion channels, the patch clamp technique [1] has become the gold standard technology for studying the cell ion channel functions in brain science and neuron science and so on [2]–[7]. As schematically shown in Fig. 1, the traditional patch clamp system usually uses a micropipette electrode, a micropipette with a micrometer-level diameter, and its tube is back-filled with the conductive solution and plugged by a silver electrode wire to contact the target cell surface and then detect the electric signals of the cell ion channels. As the electric signals of the ion channels are extremely weak, for example, the current following through ion channels is only at the picoampere level (10^{-12}A) [8]–[10], they are easily disturbed or even totally buried by environmental electric noises. To guarantee a high signal-to-noise ratio in the ion channel signal measurement, an aspiration pressure is usually imposed inside the micropipette to aspirate part of the cell membrane into the micropipette to form a giga Omega-scale seal between them (usually termed as gigaseal) for electrically shielding the environmental electronic noises [11]–[13]. As the gigaseal is the keystone to the measurement of ion channel signals in patch clamp, a higher success rate of gigaseal formation is highly desired for improving the success rate of cell patch clamp operation.

In recent years, significant advancements have been made in robotic patch clamp systems for replacing manual operations. However, according to the best of our knowledge, few of them have made significant improvements in the success rate of gigaseal formation or patch clamp operation in comparison to manual operation results. For example, the plane patch clamp system uses a microhole array connected with a pump to aspirate multiple floating cells and measure them at one time automatically [14]. However, the hole-in-plane structure makes it hard to measure adherent cell types [15]. Robotic blind cell

Manuscript received 9 May 2022; revised 29 June 2022; accepted 11 July 2022. Date of publication 25 July 2022; date of current version 3 August 2022. This work was supported in part by the National Natural Science Foundation of China under Grant 62027812 and Grant 61903201 and in part by the Beijing Advanced Innovation Center for Intelligent Robots and Systems under Grant 2019IRS05. The Associate Editor coordinating the review process was Chao Tan. *(Qili Zhao and Jinyu Qiu contributed equally to this work.) (Corresponding author: Xin Zhao.)*

Qili Zhao is with the Institute of Robotics and Automatic Information System (IRAIS) and the Tianjin Key Laboratory of Intelligent Robotic (tjKLIR), Nankai University, Tianjin 300350, China, also with the Institute of Intelligence Technology and Robotic Systems, Shenzhen Research Institute of Nankai University, Shenzhen 518083, China, and also with the Beijing Advanced Innovation Center for Intelligent Robots and Systems, Beijing Institute of Technology, Beijing 100081, China.

Jinyu Qiu, Yu Han, Yiqing Jia, Yue Du, Huiying Gong, Minghui Li, Ruimin Li, Mingzhu Sun, and Xin Zhao are with the Institute of Robotics and Automatic Information System (IRAIS) and the Tianjin Key Laboratory of Intelligent Robotic (tjKLIR), Nankai University, Tianjin 300350, China, and also with the Institute of Intelligence Technology and Robotic Systems, Shenzhen Research Institute of Nankai University, Shenzhen 518083, China (e-mail: zhaoxin@nankai.edu.cn).

This article has supplementary downloadable material available at https://doi.org/10.1109/TIM.2022.3193726, provided by the authors.

Digital Object Identifier 10.1109/TIM.2022.3193726

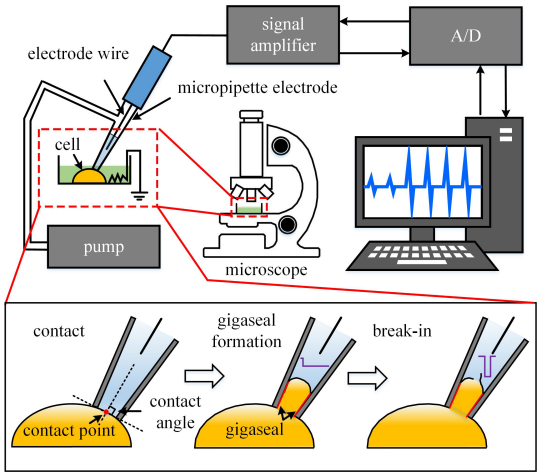

Fig. 1. Schematic of the traditional patch clamp system. The traditional patch clamp system usually uses a micropipette electrode with a micrometer-level diameter to contact the cell surface, aspirate part of the cell membrane into the micropipette to form a gigaseal between the cell surface and inner surface of the micropipette, and then measure the cell ion channel signals. To facilitate the gigaseal formation, the micropipette is preferred to contact the cell surface with a large contact angle, better close to 90°. In this way, the area of the micropipette opening covered by the cell surface after it contacts the cell membrane can be maximized before aspiration. Otherwise, the gap between the micropipette electrode and cell surface may cause gigaseal formation failures. For whole-cell patch clamp operation, the cell membrane will be broken with high negative pressure pulses (which process is usually termed as break-in) to form a whole-cell state.

patch clamp systems utilize the measured impedance of the micropipette electrode to conduct patch clamp operation on adherent cells and even cells *in vivo* automatically without visual feedback [16], [17]. However, a lack of visual guidance usually leads to lower success rates of gigaseal formation and patch clamp operation in comparison to traditional patch clamp systems. As improvements, differential interference contrast (DIC) imaging [18]–[20] and two-photon microscopy imaging [21], [22] depicting label-free neurons in brain slices and the fluorescence dye-labeled neurons in live animal brains, respectively, have been utilized to guide robotic patch clamp on these cell types. However, the operation parameters in these methods, such as the contact point selection, were still determined based on operators' experience, limiting the improvements in the success rate of gigaseal formation in comparison to manual operation results. In summary, a robotic patch clamp method with a higher gigaseal formation success rate is still desired at present.

Under the same aspiration pressure, increasing the area of the micropipette opening covered by the cell surface before aspiration can facilitate gigaseal formation. To this end, the micropipette electrode is preferred to contact the cell surface with its central axis perpendicular to the local cell surface at the contact position. This means a large contact angle between the micropipette and the cell surface (referred to as the contact angle from here on), better close to 90°, is preferred as shown in Fig. 1. At present, the operators usually control the contact angle by adjusting the tilt angle of the micropipette when it is mounted on the micromanipulator [23], which works for some special cell types with flat top surfaces. However, for common cell types with convex surfaces and complicated morphologies, this method is too rough because the differences in the contact angle across the surfaces of these cell types may be significant, even with the same tilt angle of the micropipette. For these cell types, the determination of an appropriate contact position on the cell surface is a better way to maximize the contact angle. To achieve this, 3-D morphological information of the target cell was required first.

Unfortunately, the current 3-D cell morphology measurement methods are usually not suitable to be applied in the traditional patch clamp systems due to multiple reasons. For example, 3-D cell morphology measurement methods based on atomic force microscopy (AFM) [24], [25] and scanning tunneling microscopy (STM) systems [26] rely on special probes, making them hard to be integrated with the traditional patch clamp systems. Confocal microscopy reconstructs 3-D cell morphology by capturing fluorescent cell images at different depths [27]. However, its lengthy measurement process, which usually lasts for several to tens of minutes, limits its application in patch clamp operation. In our previous research, the cell deformation generated by the contact between the micropipette tip and cell surface was detected to measure cell surface heights for fitting 3-D cell morphology [28]. However, the multiple times of contacts on the cell surface easily cause the clogging of the micrometer-size micropipette opening, which results in gigaseal formation failures, limiting its application in patch clamp operation. In summary, a noninvasive 3-D cell morphology measurement method applicable in traditional patch clamp system setup is still desired for improving the success rates of gigaseal formation.

In this article, a noninvasive 3-D cell morphology measurement method was developed to improve the success rate of gigaseal formation and patch clamp operation. First, the measured bath impedance of the micropipette electrode was modeled to get its variation trend with the micropipette tip approaching the cell surface. Using this variation trend, cell surface heights at several key points were noninvasively measured to fit 3-D cell morphology. With the obtained 3-D cell morphology, a contact point on the cell surface was determined to maximize the contact angle. Finally, a robotic whole-cell patch clamp process was established at the determined contact position to improve the success rates of gigaseal formation and the whole-cell patch clamp operation.

Experimental results on cultured human embryonic kindey (HEK)-293 cells and pyramidal neurons in mouse brain slices demonstrated that 100% and 90% success rates of noninvasive 3-D cell morphology measurements were achieved, respectively, with an average measurement error of cell surface height less than 0.15 μm. In comparison to the results at the edging point and central point which were recommended in the related work [15], [21], 36%–73% and 25%–50% increases in the success rate of gigaseal formation were achieved at the determined contact position for the above two cell types, respectively. The above advantages further led to 50%–100% and 27%–75% increases in the success rate of whole-cell patch clamp operation for the above two cell types, respectively. Furthermore, normal voltage–current relationships and action potentials were recorded on one pyramidal neuron, which was whole-cell patched by our robotic system, proving the feasibility of using our system to record the ion channel signals

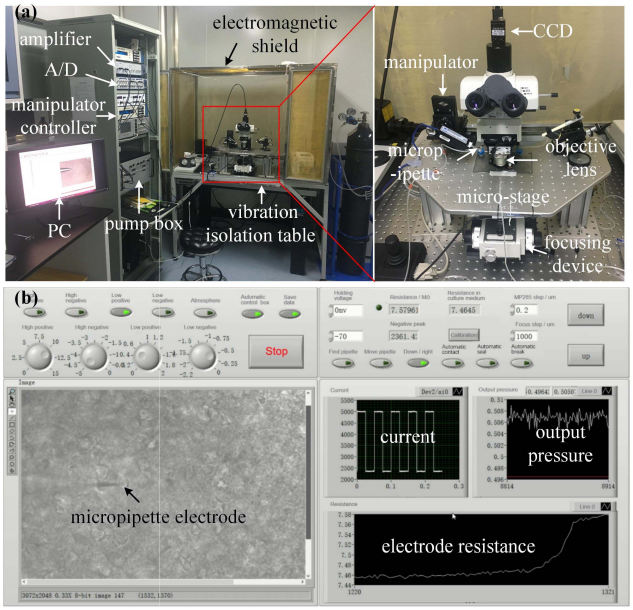

Fig. 2. System setup of the robotic patch clamp system based on noninvasive 3-D cell morphology measurement. (a) Photograph of the robotic patch clamp system. (b) Computer interface of the robotic patch clamp system.

of neurons in mouse brain slices. Our research proves the feasibility of improving the success rate of gigaseal formation for the tested two cell types based on their 3-D cell morphologies, which may spike inspiration to improve the success rates of gigaseal formation and patch clamp operation for other cell types.

II. System Setup

The robotic patch clamp system is developed within our laboratory [19]. A detailed description of the system can be found in Section I of the supplementary file "Supplementary file.docx." The system setup is shown in Fig. 2(a). An immovable stage mounted on a vibration-isolation table is utilized to position the coverslips for cell culture and brain slices. A standard upright microscope (Eclipse FN1, Nikon) capable of moving in a 2×2 cm^2 area in the XY plane with repeatability of ± 0.1 μm is utilized to observe the cells in patch clamp operation. A motorized focusing device on the microscope is utilized to autofocus the cell with a repeatability of ± 0.1 μm in the vertical direction. An X–Y–Z micromanipulator (with a travel space of $2 \times 2 \times 2$ cm^3, a maximum speed of 1 mm/s, and repeatability of ± 0.1 μm) is used to mount the micropipette electrode. An in-house developed pump box referring to [17] provides pressures inside the micropipette for patch clamp operation. The reader may find a detailed introduction to the pump box in Section II of the supplementary file "Supplementary file.docx." A charge-coupled device (CCD) camera (IR-2000, DAGE-MTI) is mounted on the microscope to acquire cell images at 60 frames per second. A host computer is used for microscopic image processing, electric signal acquisition, aspiration pressure control, and motion control for the microscope and manipulators. The whole robotic system is covered by an electromagnetic shield to isolate electric disturbances from the outside environment.

A computer interface programmed based on Labview 2018 is developed to provide visual feedback, show information about the patch clamp operation steps, display the aspiration pressure, electric signals, output pressure, and so on. Through the interface, the operator is allowed to update the patch clamp parameters, such as the aspiration pressures in patch clamp, and the moving distance of the micropipette electrode in each step. The above computer interface of the robotic patch clamp system is shown in Fig. 2(b).

The micropipette electrode utilized in the patch clamp operation is made from glass tubes (BF150-86-10, Sutter) with an inner diameter of 0.8 mm and an outer diameter of 1.5 mm. The glass tube is pulled by a micropuller (P97, Sutter) to form a micropipette with a resistance of 3–8 MΩ in the extracellular liquid. Then, the micropipette is back-filled with 20 μL of electrode liquid (mmol/L: KCl 140, NaCl 10, HEPES 10, and EGTA 5, adjusting pH to 7.3 with KOH). Before the operation, the culture medium of cells is exchanged with extracellular liquid (mmol/L: NaCl 140, KCl 4, $MgCl_2$ 2, $CaCl_2$ 2, Glucose 15, and HEPES 10, adjusting the pH to 7.4 with NaOH) for electric signal recordings. A silver electrode wire with a diameter of 0.2 mm is plugged into the micropipette to form a micropipette electrode and mounted on the manipulator with a tilt angle of 45°. The electric signals detected by the micropipette electrode are magnified by an amplifier (MultiClamp 700B, Molecular Devices), then converted to digital signals, and finally transmitted to the host computer.

III. Key Methodologies and Technologies

An electric model for the measured bath impedance of the micropipette electrode is developed to obtain its variation trend with the micropipette tip approaching the cell surface. With this variation trend, cell surface heights at several key point positions are noninvasively measured to fit the 3-D cell morphology. Based on the obtained 3-D cell morphology, a contact position on the cell surface is determined to maximize the contact angle. Furthermore, an appropriate pressing depth of the micropipette into the cell surface after contact is determined to further enlarge the cover area of the micropipette opening. Finally, a robotic whole-cell patch clamp process is established at the determined contact position to improve the success rate of gigaseal formation and the whole-cell patch clamp operation.

A. Electrical Modeling of the Measured Bath Impedance of Micropipette Electrode

The measured impedance of the micropipette electrode after it enters the extracellular liquid and before it contacts the cell surface is usually termed bath impedance [15]. As shown in Fig. 3, the measured bath impedance Z_B consists of the electrode wire impedance Z_E, the extracellular liquid impedance in the gap space between the micropipette and cell surface Z_G, the impedance of the extracellular liquid out of the gap space Z_L, and the cell impedance Z_C, which connect according to

$$Z_B = Z_E + Z_G + (Z_L || Z_C) \tag{1}$$

where "+" stands series and "||" stands parallel.

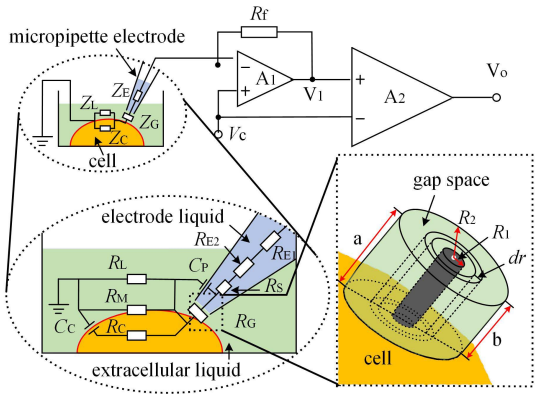

Fig. 3. Electrical model for the measured bath impedance of the micropipette electrode with it approaching cell surface.

The electrode wire impedance Z_E consists of electrode wire resistance R_{E1}, electrode liquid resistance R_{E2}, and the extra resistance R_S caused by the ion concentration gradient at the border between the electrode liquid and the extracellular liquid at the micropipette opening, which are serially connected according to

$$Z_E = R_{E1} + R_{E2} + R_S. \tag{2}$$

The cell impedance Z_C consists of cell membrane resistance R_M in parallel with cytoplasm resistance R_C serially connected cell membrane capacity C_C, which can be calculated according to

$$Z_C = R_M||(R_C + C_C). \tag{3}$$

The culture medium impedance at the gap space Z_G is mainly the resistance of the liquid in gap space denoted as R_G, and a capacitance formed by the micropipette wall denoted as C_P, which is in parallel with R_G. The extracellular liquid impedance other than the gap space Z_L is mainly the resistance of the liquid other than the gap space, which is denoted as R_L. As the capacitances can only cause a short-term transient current under the voltage patching model, they do not influence the measured bath impedance of the micropipette electrode obtained by the voltage and the steady current, which means that the capacitances can be treated as broken in the circuit of Fig. 3. According to (1) and Fig. 3, the bath resistance of the micropipette electrode R_B can be calculated according to

$$R_B = R_{E1} + R_{E2} + R_S + R_G + R_L R_M/(R_L + R_M). \tag{4}$$

Electrode wire resistance R_{E1} in (4) is a constant. To prevent the clogging issues of the micropipette electrode as it approaches the cell surface, a fine flow out of the pipette is usually generated by imposing a low positive pressure inside the micropipette. According to the calibration experimental results with the micropipette tip approaching the cell surface, the electrode liquid loss (usually less than 0.01 μL) caused by the above flow is negligible in comparison to its initial volume (about 20 μL). Thus, electrode liquid resistance R_{E2} with the micropipette electrode approaching the cell surface can be treated as a constant too. As the flow is fine and slow, the ion concentration gradient can be treated as a basic constant at the micropipette opening. Thus, the variation of R_S can be ignored with the micropipette electrode approaching the cell surface. As the variations in composition caused by the electrode liquid injected out of the micropipette and depth variations of the extracellular liquid resulting from the motion of the micropipette are ignorable in comparison to its volume (milliliter level), R_L in (4) can be treated as a constant with the micropipette tip approaching the cell surface. Before the cell is contacted and deformed by the micropipette tip, R_M and R_C can be treated as constants too. In summary, the variation trend of measured bath resistance of the micropipette electrode R_B with the micropipette electrode approaching the cell surface is mainly dependent on the variation trend of the resistance of the gap space R_G according to (4).

In the model, the gap space is defined as the extension of the micropipette opening area to the cell surface along its axis direction, which is presented as the green cylinder space in the downright inset of Fig. 3. As the inner diameter of the gap space is only about 1 μm while the size of the cell is usually larger than 10 μm, the cell surface area in the gap space is less than 1% of the total cell surface, which can be treated as a plane area without curvature. According to the experimental results, the resistance of the cell membrane (gigaohm level) is far larger than the resistance of extracellular liquid (megaohm level). Thus, the side surface of the gap space is the dominating channel for the ions flowing into and out of the micropipette rather than the cell surface. When the distance between the pipette opening and cell surface is close enough, the electric potential decrease from the micropipette opening center to the cell surface is small enough to be ignored. Based on the above assumption, a virtual cylinder superconductor shown as the black cylinder in the downright inlet of Fig. 3 can be considered to exist around the central axis of the cylinder gap space. The resistance of the extracellular liquid in the gap space R_G can be obtained according to

$$R_G = \int_{R_1}^{R_2} \rho \frac{\mathrm{d}r}{s} \tag{5}$$

where R_1 is the radius of the virtual superconductor, R_2 is the radius of the cylinder gap space, ρ is the resistivity, and s is the cross section area, which can be obtained by

$$s = \pi r(a + b) = 2\pi r d \tag{6}$$

where a and b are the highest and lowest height of the gap space (see the downright inlet of Fig. 3), respectively, and d is the distance between the micropipette opening center and cell surface along the micropipette axis direction. Thus, gap space resistance R_G can be calculated according to

$$R_G = \int_{R_1}^{R_2} \rho \frac{\mathrm{d}r}{2\pi r d} = \frac{\rho}{2\pi d} \ln \frac{R_2}{R_1}. \tag{7}$$

With the micropipette electrode approaching the cell surface along its axis direction, the decrease of d leads to an inverse increase in R_G according to (7) and, further, causes an arise in measured bath resistance of micropipette electrode R_B according to (4).

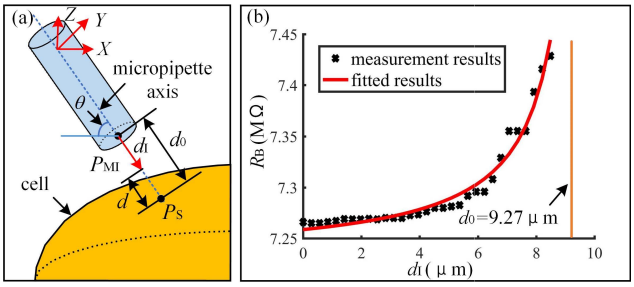

Fig. 4. Noninvasive measurement of cell surface positions based on the measured bath resistance. (a) Schematic of the measurement of 3-D cell surface position P_S. (b) Measured $[d_I(i), R_B(i)]$ and the fitted d_I–R_B curve obtained through recognized K, d_0, and R_0 ($R^2 = 0.98$).

B. Noninvasive Measurement of Cell Surface Height Based on Measured Bath Resistance

With the micropipette tip approaching the cell surface, its distance to the cell surface along its axis direction d can be obtained by

$$d = d_0 - d_I \tag{8}$$

as shown in Fig. 4(a), where d_0 is the distance between the initial position of the micropipette tip P_{MI} and cell surface along the micropipette axis direction; d_I is the moving distance of the micropipette tip from its initial position along the micropipette axis direction. According to (4), (7), and (8), the relationship between d_I and the measured bath resistance of micropipette electrode R_B can be simplified to be

$$R_B = R_0 + K/(d_0 - d_I) \tag{9}$$

where R_0 stands for the resistances serially connected with R_G in (4), which can be considered as a constant according to the analysis in Section III-A; K stands for

$$K = \frac{\rho}{2\pi} \ln \frac{R_2}{R_1}. \tag{10}$$

With the micropipette electrode approaching the cell surface step by step (with a moving step distance of 0.2 μm in this article) along its axis direction, a series of $[d_I(i), R_B(i)]$ are obtained. After each step, a least square method-based recognition method is performed to recognize K, d_0, and R_0 according to the obtained values of $[d_I(i), R_B(i)]$. Fig. 4(b) shows the measured $[d_I(i), R_B(i)]$ and the fitted d_I–R_B curve obtained through recognized K, d_0, and R_0 ($R^2 = 0.98$). When the difference in the recognized d_0 in successive three times is less than a threshold value, d_0 is determined to be the average value of them. Then, the micropipette stops approaching the cell surface immediately. The above measurement process of cell surface position is shown in the supplementary video named "video1.mp4." If contact is detected according to our previous method [28] before d_0 is confirmed, the noninvasive measurement of cell surface position is considered to be failed and the micropipette stops moving immediately.

After d_0 is confirmed, the cell surface position P_S where the micropipette tip contacts the cell surface, if it keeps moving, can be obtained by the initial position of the micropipette tip

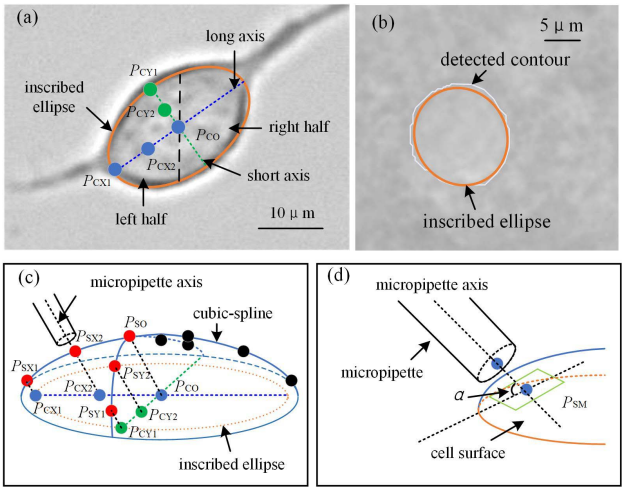

Fig. 5. Contact position determination based on the 3-D morphology of the cell. (a) Detected cell contour of HEK-293 cell using defocus imaging. (b) Obtained neuron contour based on deep study algorithms. (c) Schematic of 3-D cell morphology measurement. (d) Contact point determination based on 3-D cell morphology. The intersect point of the central axis of the micropipette electrode and cell surface is defined as P_S. The angle between the tangent plane of the cell surface at P_S and the central axis of the micropipette electrode is defined as the contact angle between the micropipette electrode and the cell surface, denoted as α. With the obtained 3-D cell morphology information, the point with the maximum value of α was defined as the contact point P_{SM}.

P_{MI} according to

$$\begin{bmatrix} x_S \\ y_S \\ z_S \end{bmatrix} = \begin{bmatrix} x_{MI} \\ y_{MI} \\ z_{MI} \end{bmatrix} + \begin{bmatrix} d_0 \cos\theta \\ 0 \\ -d_0 \sin\theta \end{bmatrix} \tag{11}$$

as shown in Fig. 4(a), where (x_S, y_S, z_S) and (x_{MI}, y_{MI}, z_{MI}) are the coordinates of P_S and P_{MI} in the world coordinate system O-XYZ, respectively; θ is the tilting angle of the micropipette to the horizontal plane. Here, the micropipette is mounted with its central axis parallel with the XZ plane before measurements. The cell surface height at P_S is obtained from the vertical position difference between it and the focus plane (see Section III-C).

According to (11), the 3-D position of the micropipette electrode tip P_{MI} (x_{MI}, y_{MI}, z_{MI}) needs to be localized first to get the 3-D position of the cell surface P_S (x_S, y_S, z_S). For aspiration of the top cell surface, and meanwhile, not occluding the view, the micropipette electrode for the traditional patch clamp is usually mounted with a tilting angle θ, leading to significant differences in the focus state across the micropipette body. Thus, the traditional recognition methods for micropipettes parallel to the horizontal plane [29]–[31] are not suitable to localize the tilt micropipette in the patch clamp. To address this problem, a 3-D localization algorithm of the tilt micropipette tip based on the contour length of the micropipette electrode is proposed in this article. The reader may find a detailed introduction of this method in Section III of the uploaded supplementary file "Supplementary file.docx."

C. Noninvasive 3-D Cell Morphology Measurement

Before cell surface height measurement, the cell contour in the XY plane is localized using image processing algorithms. For cultured adherent cells, they are first autofocused and

then localized to get their contours in the *XY* plane using the defocusing imaging-based method in our previous research [19], [32]. For neurons in mouse brain slices, due to their blur contours, they are first manually focused and then localized using deep learning algorithms reported in [18] to get their contours in the *XY* plane. Then, inscribed ellipses of their contours are fitted, as shown in Fig. 5(a) and (b). For the cells with convex shapes, their top points are usually above the central points of cell contours P_{CO}. As the tilting micropipette is mounted on the left hand of the manipulator and parallel with the *XZ* plane in this article, the left half cell surface likes the upslope of the "mountain cell." The contact angles between the micropipette and the left half-cell surface are usually larger than those at the right half-cell surface. Thus, the cell surface point maximizing the contact angle is usually on the left half cell surface, making 3-D morphology measurement of the right half cell surface not necessary.

To measure the 3-D morphology of the left half cell surface, three points evenly distributed on the half long axis (P_{CX1}, P_{CX2}, and P_{CO}) and three points evenly distributed on the half short axis of the left half of the inscribed ellipse (P_{CY1}, P_{CY2}, and P_{CO}) are selected as the five target points of micropipette tip to approach. During approaching the above points, five points on the left half cell surface (P_{SX1}, P_{SX2}, P_{SY1}, P_{SY2}, and P_{SO}) are detected noninvasively [red points in Fig. 5(c)] according to the method in Section III-B. Assuming the cell surface is symmetric to the two vertical planes containing the short axis and long axis, three points mirroring P_{SX2}, P_{SX1}, and P_{SO} and two points mirroring P_{SY1} and P_{SY2} are automatically generated on the right half cell surface [black points in Fig. 5(c)]. Then, the two cell surface curves above the long axis and short axis are obtained through the cubic-spline fitting of the above ten points, as shown in Fig. 5(c). After that, 24 points evenly distributed on the above two cubic-spine curves (12 points on each curve besides) are selected to fit the 3-D cell surface through a fourth polynomial.

D. Determination of the Contact Position and Pressing Depth for a Higher Success Rate of Gigaseal Formation

The contact angle between the micropipette electrode and the cell surface is defined to be the angle between the tangent plane of the cell surface at the contact point and the central axis of the micropipette electrode, which is denoted as α in Fig. 5(d). With the obtained 3-D cell morphology, the system then scans the whole cell surface to determine a position with the maximum contact angle [see P_{SM} in Fig. 5(d)] as the contact position in the following patch clamp for a higher success rate of gigaseal formation.

After the micropipette electrode tip contacts the cell surface at the determined position, it still needs to press the cell surface by a certain distance to further enlarge the micropipette opening area covered by the cell surface. The pressing depth needs to be chosen carefully, neither too small to cover the micropipette opening nor too large leading to cell membrane penetration. To save the length of this article, the determination of the above appropriate pressing depth has been provided in Section IV of the uploaded supplementary file "Supplementary file.docx."

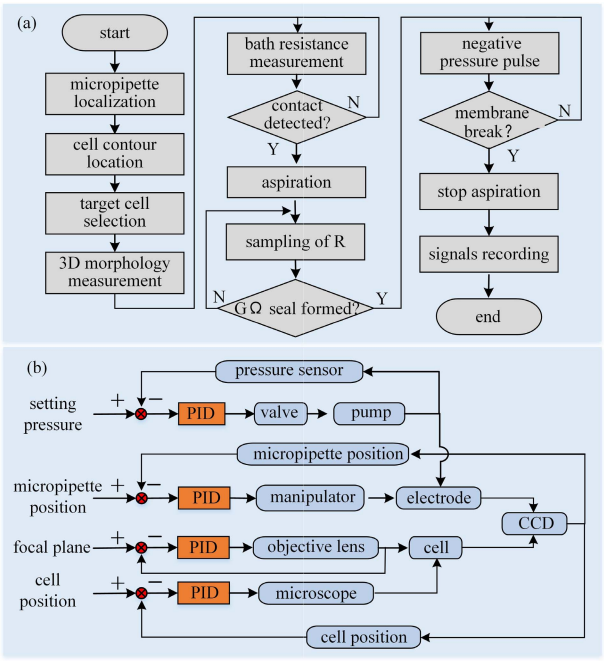

Fig. 6. Robotic whole-cell patch clamp process based on noninvasive 3-D cell morphology measurement. (a) Operation flow of the robotic whole-cell patch clamp process. (b) Control diagram of the robotic whole-cell patch clamp system.

E. Robotic Whole-Cell Patch Clamp Based on 3-D Cell Morphology Measurement

Based on the above work, a robotic whole-cell patch clamp process is established at the determined position to increase the success rate of gigaseal formation and whole-cell patch clamp operation. The robotic whole-cell patch clamp operation procedure is summarized in Fig. 6(a). After the cover slide with HEK293 cells or the mouse brain slice is placed on the stage, the micropipette electrode is manually moved into the field of view above the extracellular liquid surface. Then, the robotic whole-cell patch clamp operation started.

First, the electrode moves downward to approach the extracellular liquid surface automatically. When the measured micropipette electrode resistance reduces to 3–8 MΩ, the micropipette electrode is considered to enter the extracellular liquid. Then, the micropipette electrode is automatically localized to get its 3-D position as mentioned in Section III-B. Furthermore, it is moved out of view to exclude its disturbances to the following cell contour detection. Furthermore, the system lowers down the objective lens and micropipette simultaneously to focus and then localize the cells. Then, the micropipette electrode moves into the view again and then approaches the five target points mentioned in Section III-C along the micropipette axis direction to measure the 3-D morphology of the selected target cell. Furthermore, the contact position on the cell surface maximizing the contact angle is determined based on the measured 3-D cell morphology.

After that, the micropipette electrode moves downward to contact the cell surface at the determined position. During this process, a low positive pressure of 0.5 psi is applied inside the micropipette to generate a fine flow out of the micropipette opening for reducing clogging issues. A clogging

issue is considered to occur if a rapid increase in the measured bath resistance (by larger than 1 MΩ in 1 s) is found and the measured bath resistance does not decrease when the micropipette moves backward. A large positive pressure pulse with an amplitude of 10 psi and a duration of 1 s is then applied inside the micropipette to break the clogging. If the bath resistance decreases to its previous level, which means that the clogging materials at the tip had been removed, the micropipette electrode continues to move downward. Else, the micropipette tip is considered to be clogged totally and replaced with a new one. Then, the above processes are repeated.

After the micropipette arrives at the target contact position, it moves downward by a certain distance (1 μm in this article, see more details in Section IV of the uploaded supplementary file "Supplementary file.docx") to press into the cell surface for enlarging its covered area. Then, system switches the former low positive pressure to a low negative aspiration pressure to form the gigaseal. An effective gigaseal is considered to be formed if the measured micropipette electrode impedance increases up to 1 GΩ in 2 min. Otherwise, the attempt is considered to be failed. During the gigaseal formation process, a too-small aspiration pressure is not able to form a gigaseal, while a too-large one may break the cell membrane before gigaseal formation. The appropriate aspiration pressure is experimentally determined to be −0.5 psi.

After the gigaseal is formed, negative pressure pulses with an amplitude of −5 psi and a duration of 1 s are repeatedly exerted inside the micropipette to break part of the cell membrane aspirated in the micropipette (break-in), forming a whole-cell state before signal recordings. The measured resistance of the micropipette electrode, which usually decreases to less than 500 MΩ after break-in, is measured online to judge whether the break-in occurs. If the membrane breaks within less than six pulses, a successful break-in and whole-cell patch clamp operation are conducted. Otherwise, the attempt is considered to be failed. The reader can find more details about the gigaseal formation and break-in process in the supplementary video named "video2.mp4."

During the above robotic patch clamp operation process, the microscope, objective lens, and micropipette electrode are moved coordinately to "move" the target cell to the field of view and move the micropipette electrode tip to approach or contact the cell surface. The PID controllers are designed to control the motion of the micropipette electrode, microscope, and focus device and adjust the pressures inside the micropipette. The control diagram of the robotic patch clamp system is shown in Fig. 6(b).

IV. Experimental Results

A series of experiments on HEK-293 cells and pyramidal neurons in the visual cortex of brain slices were conducted to validate the effectiveness of the research in this article. The preparations of the above two cell types have been given in Section V of the uploaded supplementary file "Supplementary file.docx." All animal experiments were approved by the Experimental Animal Ethics Committee, Nankai University, and were performed following the Animal Management Rules of the Ministry of Health of the People's Republic of China. First, the 3-D localization for ten micropipettes was performed to evaluate the localization accuracy of the proposed tilt micropipette localization method in Section III-B. Then, the cell surface heights at the aforementioned five key points were measured using the proposed noninvasive method and benchmarked by the previous-developed contact detection-based method and the AFM-based method. Finally, the success rates of gigaseal formation and whole-cell patch clamp operation at the determined contact point maximizing contact angle were compared with the results at the other two points recommended in other references.

TABLE I
Robotic Localization Errors of Ten Micropipette Electrodes

Micropipette	Localization error (μm)	Measurement time (s)
1	0.27±0.10	8.45±3.79
2	0.50±0.06	8.82±2.19
3	0.35±0.10	10.48± 2.26
4	0.41±0.06	7.97±2.05
5	0.40±0.12	6.64±0.52
6	0.24±0.17	7.12±1.65
7	0.29±0.06	12.02±2.26
8	0.35±0.21	10.18±2.62
9	0.34±0.20	8.78±3.04
10	0.36±0.08	8.11±0.81

A. Localization Results for Tilt Micropipette Electrode Tip

As mentioned in Section III-B, the 3-D localization results of the micropipette electrode tip have significant influences on the measurement accuracy of the 3-D cell morphology. Thus, ten micropipette electrodes were randomly selected to evaluate the errors of the proposed 3-D micropipette tip localization method. For each micropipette electrode, it was autofocused and then localized automatically, repeated three times. The experimental results are summarized in Table I. All ten micropipette tips were successfully focused and localized in all 30 tests (with a success rate of 100%). The average time cost in the robotic micropipette tip localization is only 9.20 ± 2.70 s ($n = 30$), which is mainly the cost in the autofocusing process. The obtained 3-D tip positions were benchmarked by the manually input ones by clicking the mouse at the tips after manual focus. The distance between them is defined as 3-D localization errors. The average localization error is only 0.35 ± 0.13 μm ($n = 30$). These errors are mainly caused by the resolution limitation of the microscopic imaging, which was 0.12 μm/pixel under the 40× objective lens, and the autofocus error. These errors are negligible in comparison to the sizes of HEK-293 cells and neurons (usually more than 10 μm according to observation results), laying a solid foundation for the following precise measurement of 3-D cell morphology.

B. Noninvasive 3-D Morphology Measurement Results for Cells

A total number of ten HEK-293 cells in five glass coverslips (two cells on each coverslip) and ten pyramidal neurons in

the visual cortex of five brain slices (two neurons in each slice) obtained from five mice, respectively, were randomly selected for the experiments. These cells were first tested by the proposed noninvasive 3-D cell morphology measurement method and then by our previous contact detection-based 3-D cell morphology measurement method [28]. The clogging rate and the measured cell surface heights by two methods were compared to validate the effectiveness of the noninvasive 3-D cell morphology measurement method. Furthermore, the measured cell surface heights by the above two methods were benchmarked by the 3-D cell morphology measured by the AFM (Resolve, Bruker) to evaluate the measurement errors of cell surface height of the above two methods. The reader may find more details about the protocols of the 3-D cell morphology measurement using noninvasive method, contact detection method, and the AFM-based method in Section VI of the uploaded supplementary file "Supplementary file.docx."

1) *Success Rate of Noninvasive 3-D Cell Morphology Measurement:* The clogging occurrence rates in the above two measurement methods were compared to evaluate the success rate of our noninvasive measurement method. For the contact detection-based method, there were seven and eight clogging incidences occurred in the measurement of ten HEK-293 cells and ten pyramidal neurons, respectively. In comparison, none and only one clogging incidence occurred during the noninvasive measurement of ten HEK-293 cells and ten pyramidal neurons, respectively. This advantage is mainly because the variation of measured bath impedance used to noninvasively locate cell surface height occurs before the micropipette contacts the cell surface while the cell deformation occurs after the contact, as shown in Fig. 7(a). In the ten and nine successful noninvasive cell morphology measurements on the above two types of cells, there was no contact detected through image processing. For the one clogging case for pyramidal neuron, the contact between the micropipette tip and cell surface was detected, which mainly resulted from the recognition error of distance to the cell surface [d_0 in (8)] due to bath resistance measurement errors. In summary, the success rates of noninvasive 3-D cell morphology measurement for cultured HEK-293 cells and pyramidal neurons in the visual cortex of the mouse brain slices are 100% (10/10) and 90% (9/10), respectively.

2) *Calibration Experiments on the Measured Cell Surface Heights:* Fig. 7(b) summarizes the differences between the measured cell surface heights by our noninvasive method and the contact detection-based method at P_{SX1}, P_{SX2}, P_{SO}, P_{SY1}, and P_{SY2} [see Fig. 5(c)] on two types of cells, respectively. It can be found that the measured cell surface heights using the noninvasive method are higher (the value of the bar is larger than zero) by 0.3–0.6 μm than those obtained by the contact detection-based method at every point on both two types of cells. This is mainly because the contact detection-based method requires the micropipette tip to press into the cell surface by a certain depth to generate detectable cell deformation by image processing, causing the measured cell surface lower than its normal state. Furthermore, it is worthy to note that the above differences in HEK-293 cells are smaller than those of neuron cells, as shown in Fig. 7(b).

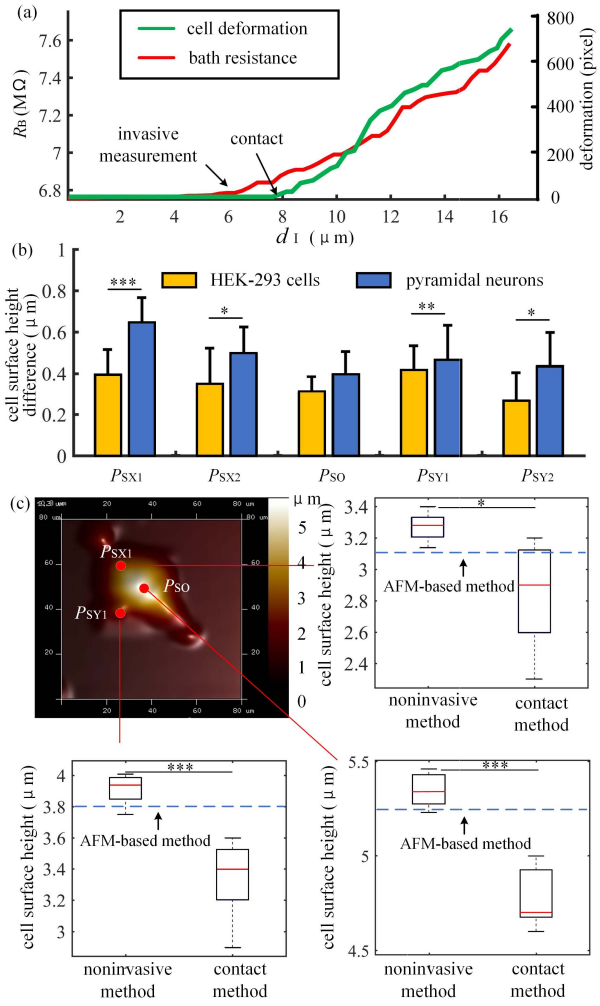

Fig. 7. 3-D cell morphology measurement results. (a) Obtained variation trend of bath resistance of micropipette electrode and cell deformation with the micropipette tip approaching the cell surface. The rise of the bath resistance occurs before the generated cell deformation with the micropipette electrode approaching the cell surface. (b) Differences in measured cell surface height of two types of cells at the five key points using the proposed noninvasive method and the contact detection-based method. The differences for cultured HEK-293 cells were larger than those of pyramid neurons in mouse brain slices ($P^{***} = 0.000164$ at P_{SX1}, $P^{*} = 0.01977$ at P_{SX2}, $P = 0.21943$ at P_{SO}, $P^{**} = 0.009197$ at P_{SY1}, and $P^{*} = 0.020879$ at P_{SY2}). (c) HEK-293 cell surface height measured by the AFM-based method, contact detection-based method, and noninvasive method at P_{SX1}, P_{SY1}, and P_{SO}. The measurement errors between the noninvasive method and AFM-based method are much smaller than the errors between the contact detection-based method and AFM-based method (0.17 ± 0.10 μm versus -0.26 ± 0.36 μm at P_{SX1}, 0.15 ± 0.09 μm versus -0.42 ± 0.16 μm at P_{SO}, and 0.11 ± 0.10 μm versus -0.46 ± 0.27 μm at P_{SY1}).

This is mainly because the background of neurons in brain slices (brain tissues) is softer than that of cultured HEK-293 cells (glass coverslips). In comparison to HEK-293 cells, the micropipette tip needs to press into the neuron surface by a larger depth to generate a detectable cell deformation through image processing methods.

To further compare the measurement accuracies of the above two methods, the 3-D morphology of one HEK-293 cell was measured by AFM to benchmark the cell surface heights obtained by the above two methods. Fig. 7(c) shows the obtained 3-D cell morphology by AFM-based method and the

measured cell surface heights at P_{SX1}, P_{SY1}, and P_{SO} using the noninvasive method and contact detection-based method (repeated five times at each point). The average measurement error of cell surface height between our noninvasive method and the AFM-based method is less than 0.15 μm, which is about 3% of the cell height of HEK-293 cells (usually about 5 μm), laying a solid foundation for precise measurement of 3-D cell morphology.

It can be found that the average errors between the cell heights measured by our noninvasive method and the ones measured by the AFM-based method are smaller than those between the contact detection-based method and AFM-based method at all the above three points [0.17 $\pm$ 0.10 μm ($n = 5$) versus -0.26 ± 0.36 μm ($n = 5$) at P_{SX1} ($P^* = 0.026$), 0.15 $\pm$ 0.09 μm ($n = 5$) versus -0.42 ± 0.16 μm ($n = 5$) at P_{SO} ($P^{***} = 0.0002$), and 0.11 $\pm$ 0.10 μm ($n = 5$) versus -0.46 ± 0.27 μm ($n = 5$) at P_{SY1}($P^{**} = 0.003$)]. This advantage is interesting because, in comparison to our noninvasive method, both the AFM-based method and contact detection-based method are invasive. The AFM-based method utilizing the generated force to measure cell surface height may be more sensitive than the contact detection-based method utilizing the cell surface deformation to measure the cell surface height. That may be the reason why the cell surface heights measured by the AFM-based method are higher than those of the contact detection-based method and closer to the measured results by our noninvasive method, as shown in Fig. 7(c). Besides the average measurement error, it can be found that the standard deviation of the measurement error of the proposed method (less than 0.1 μm on average) is also significantly smaller than that of the contact detection-based method (0.26 μm on average). This means that the proposed noninvasive method has better repeatability than the contact detection method, which is vital for 3-D cell morphology measurement.

C. Robotic Whole-Cell Patch Clamp Results Based on 3-D Cell Morphology Measurement

A total number of 90 HEK-293 cells cultured on three glass coverslips and 60 pyramidal neurons in the visual cortex of six mouse brain slices from six mice were prepared for the experiments. Both the 90 cultured HEK-293 cells and 60 pyramidal neurons were randomly divided into three groups (30 cells and 20 cells in each group, respectively). Besides P_{SM}, the edging point of cell surface P_{SE} (which is located at the P_{SX1} in the experiment) and the central point of cell contour on the cell surface P_{SC}, which were recommended in [15] and [21], were selected as contact positions between the micropipette and cell surface to conduct robotic whole-cell patch operation. The recorded resistances of the micropipette electrode and the imposed pressures inside the micropipette in the whole-cell patch clamp operation are shown in Fig. 8(b) and (c), respectively. The contact point settings, success rates of gigaseal formation, and whole-cell patch clamp for each group of cells are summarized in Table II.

It can be found that the highest success rates of gigaseal formation and whole-cell patch clamp operation were achieved

TABLE II
ROBOTIC WHOLE-CELL PATCH CLAMP OPERATION RESULTS

Group	Cell types	Contact points	Gigaseal formation	Whole-cell patch clamp	Operation time (s)
1	HEK-293 cells	P_{SE}	11/30 (36.67%)	9/30 (30.00%)	181$\pm$27 (n=9)
2		P_{SC}	14/30 (46.67%)	12/30 (40.00%)	185$\pm$18 (n=12)
3		P_{SM}	19/30 (63.33%)	18/30 (60.00%)	247$\pm$29 (n=18)
1	pyramidal neurons	P_{SE}	10/20 (50.00%)	8/20 (40%)	207$\pm$31 (n=8)
2		P_{SC}	12/20 (60.00%)	11/20 (55.00%)	196$\pm$22 (n=11)
3		P_{SM}	15/20 (75.00%)	14/20 (70.00%)	267$\pm$27 (n=14)

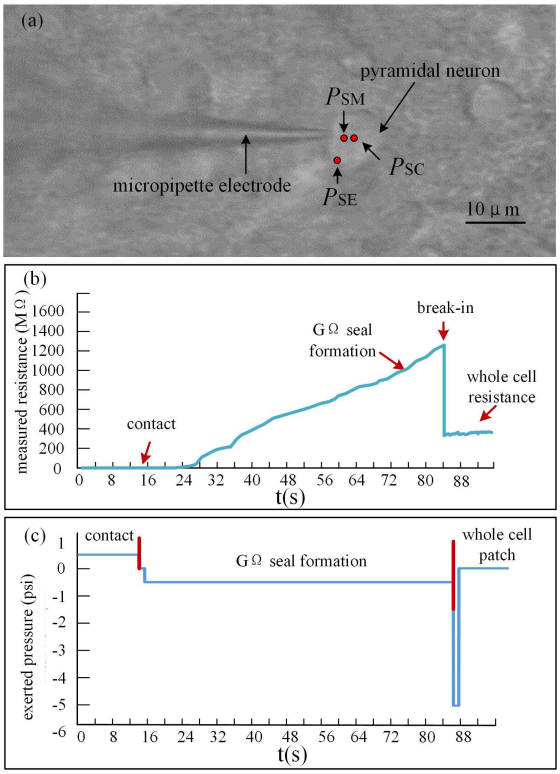

Fig. 8. Whole-cell patch clamp operation for the pyramidal neurons in the visual cortex of the mouse brain slices. (a) Experimental picture of whole-cell patch clamp for pyramidal neurons. (b) and (c) Exerted pressure and measured electrode resistance during the robotic whole-cell patch clamp process.

at the determined contact position P_{SM} for both two cell types. With the maximized contact angle, the success rate of the gigaseal formation at P_{SM} was improved by 36%–73% and 25%–50% for the above two cell types, respectively, in comparison to the success rate at the other two points. This advantage leads to 50%–100% and 27%–75% increases in whole-cell patch clamp operation. Furthermore, the success rate of the whole-cell patch clamp using our method (60% for HEK293 cells and 70% for pyramidal neurons in the visual cortex of mouse brain slices) is also higher than the 40%–50% success rate of the previous automated patch clamp systems in [18] and [33] under whole-cell recording configuration. The above results demonstrate that in comparison to the edging point and the central point of the cell surface, the determined contact position is capable of significantly improving the

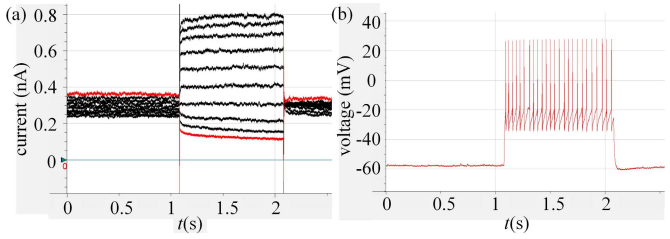

Fig. 9. Recorded ion channel signals of one pyramidal neuron in the visual cortex of mouse brain slice. (a) Voltage-clamp traces from the neuron in the visual cortex during voltage injection (1000-ms-long pulses from −30 to 60 mV in 10-mV steps). (b) Current-clamp recording with a 1000-ms-long current injection pulse at 150 pA. Normal periodic action potentials were detected.

success rate of gigaseal formation and whole-cell patch clamp for the above two cell types. With the involvement of the extra process of 3-D cell morphology measurement, which is requisite for the determination of P_{SM}, the average time cost for whole-cell patch clamp operation at P_{SM} is increased by about 1 min on average in comparison to the operation time at the other two points, which can be directly determined by the detected cell contour without 3-D cell morphology measurement.

Furthermore, the ion channel signals of one pyramidal neuron in the V1 pyramidal cell layer were recorded after the whole-cell patch clamp operation was conducted on it. The voltage-clamp traces during voltage injection (1000-ms-long pulses from −30 to 60 mV in 10-mV steps) and current-clamp recording with a 1000-ms-long current injection pulse at 150 pA were conducted with recorded signals shown in Fig. 9. From Fig. 9(a), normal voltage–current relationships were found when injected voltage varied from −30 to 60 mV. Furthermore, normal action potentials triggered by the current injection pulse were detected in Fig. 9(b). The above results demonstrated the feasibility of using our robotic patch clamp system to record the ion channel signals of pyramidal neurons in the visual cortex of the mouse brain slices.

V. Discussion

In this article, the 3-D cell morphology information was noninvasively measured to determine a contact point to facilitate the gigaseal formation and, meanwhile, prevent clogging issues of the micropipette electrode. The experimental results demonstrate that significant improvements in the success rate of gigaseal formation have been achieved at the determined contact point maximizing the contact angle in comparison to the results at the points recommended in other references. With the appropriate contact position, the pressing depth of the micropipette electrode into the cell surface requisite for covering the micropipette opening was reduced to 1 μm, and thereby, no cell penetration incidences was found in the whole-cell patch clamp operation of all 90 cultured HEK-293 cells and 60 pyramidal neurons. Our research may provide a new sight to improve the success rate of gigaseal formation and the whole-cell patch clamp operation through contact position selection based on the cell morphology information.

As mentioned before, the measured electric signals by patch clamp system can be easily disturbed by the environmental electronic noise. In order to reduce their disturbances to the measured resistance in this article, the following measures have been made in the patch clamp operation. First, the extracellular solution, where the target cells or mouse brain slices are immersed, and the surface of our robotic patch clamp system are electrically grounded. Second, the whole robotic system is covered by an electromagnetic shield to isolate environmental electronic noise. Third, the recorded resistances are filtered by the software to reduce electronic noise. Furthermore, with a higher success rate of gigaseal formation achieved in this article, the disturbance of the environmental electronic noise to the measured signals can be reduced besides the current grounding, shielding, filtering methods, and any other possible hardware upgrading of the system [34] in the future.

In this article, the 3-D cell morphology was fitted according to the measured cell surface heights at five points. Certainly, increasing the number of testing points on the cell surface may fit a more detailed 3-D cell morphology determining a more precise cell surface point maximizing contact angle. However, the increase in the testing point number will further slow down the whole-cell patch clamp operation. With the involvement of the cell surface height measurement process at the above five points, which usually costs about 1 min on average, the operation speed of our method is already slower than the traditional method. The robotic whole-cell patch clamp operation speed can be accelerated by increasing the automation level of our system in the future. For example, the automated searching algorithm for micropipette may be developed to save the time cost in manual searching and positioning of the micropipette in patch clamp. Besides, the replacement process of the micropipette electrode, including the remounting and repositioning of the micropipette electrode, which usually costs 3–5 min in total, significantly slows down the whole-cell patch clamp operation speed when clogging issues of the micropipette occur. Kolb *et al*. [34] introduced a micropipette washing method for micropipette electrode reuse. A similar module for automated washing of micropipette electrodes will be added to the proposed system to accelerate whole-cell patch clamp operations in the future.

It is desirable to test our system and methods on alternative cell lines in the future. In comparison to the HEK-293 cells, the primary (neuronal) dissociate cells are more appropriate adherent cell lines to test the performance of our robotic patch clamping system on adherent cells, especially considering that the other cell type tested in this article were neurons in brain slices. In that way, more objective comparisons can be made between the patch clamp results of our system on culture neurons and neurons in the brain slices. Besides the pyramidal neurons in the visual cortex, more types of neurons in the mouse brain slices are expected to be operated and their ion channel signals will be measured to test the performance of our system in the ion channel signal recordings for neurons.

The AFM-based 3-D cell morphology measurement for adherent cells is challenging, not to mention the measurement

of neurons in brain slices. Only one HEK-293 cell was measured by AFM to benchmark the proposed method in this article at present. As the improvement of our operation skills, more 3-D cell morphology measurements based on AFM are expected to be performed on adherent cells or even neurons in brain slices in the future to further validate the measurement accuracy of our noninvasive 3-D cell morphology measurement method.

VI. Conclusion

This article presented a robotic patch clamp method based on noninvasive 3-D cell morphology measurement for a high success rate of gigaseal formation, which is requisite in ion channel signal recordings. The measured bath resistance of the micropipette electrode was modeled to measure 3-D cell morphology noninvasively with a measurement success rate of 90% and a measurement error of cell surface height less than 0.15 μm. With the obtained 3-D cell morphology, the contact position on the cell surface maximizing the contact angle is determined for a higher success rate of gigaseal formation. At the determined contact position, the success rates of gigaseal formation for HEK-293 cells and pyramidal neurons in the visual cortex of the mouse brain slices are improved by 36%–73% and 25%–50%, respectively, in comparison to the results at the two points recommended in related work. With a higher success rate of gigaseal formation, the success rates of whole-cell patch operation for the above two cell types are improved by 50%–100% and 27%–75%, respectively. Our research may spike the inspiration to improve the success rate of gigaseal formation and the whole-cell patch clamp operation according to the 3-D cell morphology information.

References

[1] E. Neher and B. Sakmann, "Single-channel currents recorded from membrane of denervated frog muscle fibres," *Nature*, vol. 260, no. 5554, pp. 799–802, Apr. 1976.

[2] Y. Peng, F. X. Mittermaier, H. Planert, U. C. Schneider, H. Alle, and J. R. P. Geiger, "High-throughput microcircuit analysis of individual human brains through next-generation multineuron patch-clamp," *eLife*, vol. 8, Nov. 2019, Art. no. e48178.

[3] A. Marques-Smith *et al.*, "Recording from the same neuron with high-density CMOS probes and patch-clamp: A ground-truth dataset and an experiment in collaboration," *bioRxiv*, vol. 10, pp. 1–66, Jan. 2020.

[4] K. Otomo, J. Perkins, A. Kulkarni, S. Stojanovic, J. Roeper, and C. A. Paladini, "*In vivo* patch-clamp recordings reveal distinct subthreshold signatures and threshold dynamics of midbrain dopamine neurons," *Nature Commun.*, vol. 11, no. 1, pp. 1–15, Dec. 2020.

[5] G. L. Holst *et al.*, "Autonomous patch-clamp robot for functional characterization of neurons *in vivo*: Development and application to mouse visual cortex," *J. Neurophysiol.*, vol. 121, no. 6, pp. 2341–2357, Jun. 2019.

[6] A. Kokhan, S. Zdanevich, I. Prokofev, I. Gorudko, and E. Shamova, "Patch-clamp technique for studying ion channels in activated platelets," *Syst. Biol. Physiol. Rep.*, vol. 1, no. 1, pp. 3–11, Mar. 2021.

[7] L. A. Annecchino and S. R. Schultz, "Progress in automating patch clamp cellular physiology," *Brain Neurosci. Adv.*, vol. 2, May 2018, Art. no. 239821281877656.

[8] H. M. Keizer *et al.*, "Functional ion channels in tethered bilayer membranes—Implications for biosensors," *ChemBioChem*, vol. 8, no. 11, pp. 1246–1250, Jul. 2007.

[9] R. W. Aldrich, "A new standard: A review of *handbook of ion channels*," *J. Gen. Physiol.*, vol. 146, no. 2, pp. 21–119, Aug. 2015.

[10] L. S. Liebovitch and J. P. Koniarek, "Ion channel kinetics," *IEEE Eng. Med. Biol. Mag.*, vol. 11, no. 2, pp. 53–56, Jun. 1992.

[11] R. I. Slavchov, T. Nomura, B. Martinac, M. Sokabe, and F. Sachs, "Gigaseal mechanics: Creep of the gigaseal under the action of pressure, adhesion, and voltage," *J. Phys. Chem. B*, vol. 118, no. 44, pp. 12660–12672, Nov. 2014.

[12] A. Verkhratsky and V. Parpura, "History of electrophysiology and the patch clamp," in *Patch-Clamp Methods and Protocols* (Methods in Molecular Biology), vol. 1183. New York, NY, USA: Humana Press, 2014, pp. 1–19.

[13] H.-J. Suk, E. S. Boyden, and I. van Welie, "Advances in the automation of whole-cell patch clamp technology," *J. Neurosci. Methods*, vol. 326, Oct. 2019, Art. no. 108357.

[14] A. Obergrussberger *et al.*, "Automated patch clamp meets high-throughput screening: 384 cells recorded in parallel on a planar patch clamp module," *SLAS Technol.*, vol. 21, no. 6, pp. 779–793, Dec. 2016.

[15] Z. Liu, *Practical Patch Clamp Techniques*, 2nd ed. Beijing, China Beijing Science and Technology Press, 2016.

[16] W. A. Stoy *et al.*, "Robotic navigation to subcortical neural tissue for intracellular electrophysiology *in vivo*," *J. Neurophysiol.*, vol. 118, no. 2, pp. 1141–1150, Aug. 2017.

[17] S. B. Kodandaramaiah *et al.*, "Assembly and operation of the autopatcher for automated intracellular neural recording *in vivo*," *Nature Protocols*, vol. 11, no. 4, pp. 634–654, Mar. 2016.

[18] K. Koos *et al.*, "Automatic deep learning-driven label-free image-guided patch clamp system," *Nature Commun.*, vol. 12, no. 1, p. 936, Feb. 2021.

[19] Q. Zhao, Y. Han, Y. Jia, N. Yu, M. Sun, and X. Zhao, "Robotic whole-cell patch clamping based on three dimensional location for adherent cells," in *Proc. Int. Conf. Manipulation, Autom. Robot. Small Scales (MARSS)*, Jul. 2020, pp. 1–6.

[20] J. Lee, I. Kolb, C. R. Forest, and C. J. Rozell, "Cell membrane tracking in living brain tissue using differential interference contrast microscopy," *IEEE Trans. Image Process.*, vol. 27, no. 4, pp. 1847–1861, Apr. 2018.

[21] H. J. Suk, I. V. Welie, S. B. Kodandaramaiah, B. Allen, C. R. Forest, and E. S. Boyden, "Closed-loop real-time imaging enables fully automated cell-targeted patch-clamp neural recording *in vivo*," *Neuron*, vol. 95, no. 5, pp. 1037–1047, Aug. 2017.

[22] L. A. Annecchino, A. R. Morris, C. S. Copeland, O. E. Agabi, P. Chadderton, and S. R. Schultz, "Robotic automation of *in vivo* two-photon targeted whole-cell patch-clamp electrophysiology," *Neuron*, vol. 95, no. 5, pp. 1048–1055, Aug. 2017.

[23] K. Koos, J. Molnár, and P. Horvath, "Pipette Hunter: Patch-clamp pipette detection," in *Proc. Scand. Conf. Image Anal.*, vol. 10269, May 2017, pp. 172–183.

[24] M. A. Selimov *et al.*, "Investigation of $CdCl_2$ influence on red blood cell morphology," *Int. J. Pharmaceutical Phytopharmacol. Res.*, vol. 9, no. 5, pp. 8–13, 2019.

[25] C. Petit *et al.*, "Visuo-haptic virtual exploration of single cell morphology and mechanics based on AFM mapping in fast mode," *J. Micro-Bio Robot.*, vol. 16, no. 2, pp. 147–160, Dec. 2020.

[26] S. Sahare, P. Ghoderao, S. B. Khan, Y. Chan, and S.-L. Lee, "Recent progress in hybrid perovskite solar cells through scanning tunneling microscopy and spectroscopy," *Nanoscale*, vol. 12, no. 30, pp. 15970–15992, Aug. 2020.

[27] L. Oliveira-Soto and N. Efron, "Morphology of corneal nerves using confocal microscopy," *Cornea*, vol. 20, no. 4, pp. 374–384, May 2001.

[28] J. Liu *et al.*, "Automated robotic measurement of 3-D cell morphologies," *IEEE Robot. Autom. Lett.*, vol. 2, no. 2, pp. 499–505, Apr. 2017.

[29] Q. Zhao, M. Sun, M. Cui, J. Yu, Y. Qin, and X. Zhao, "Robotic cell rotation based on the minimum rotation force," *IEEE Trans. Autom. Sci. Eng.*, vol. 12, no. 4, pp. 1504–1515, Oct. 2015.

[30] Z. Lu, X. Zhang, C. Leung, N. Esfandiari, R. F. Casper, and Y. Sun, "Robotic ICSI (intracytoplasmic sperm injection)," *IEEE Trans. Biomed. Eng.*, vol. 58, no. 7, pp. 2102–2108, Jul. 2011.

[31] J. Krabicka and Y. Yan, "Finite-element modeling of electrostatic sensors for the flow measurement of particles in pneumatic pipelines," *IEEE Trans. Instrum. Meas.*, vol. 58, no. 8, pp. 2730–2736, Aug. 2009.

[32] W. Dou *et al.*, "Label-free conduction velocity mapping and gap junction assessment of functional iPSC-cardiomyocyte monolayers," *Biosensors Bioelectron.*, vol. 167, Nov. 2020, Art. no. 112468.

[33] L. Li *et al.*, "A robot for high yield electrophysiology and morphology of single neurons *in vivo*," *Nature Commun.*, vol. 8, no. 1, pp. 1–10, Jun. 2017.

[34] I. Kolb, W. A. Stoy, E. B. Rousseau, O. A. Moody, A. Jenkins, and C. R. Forest, "Cleaning patch-clamp pipettes for immediate reuse," *Sci. Rep.*, vol. 6, no. 1, p. 35001, Oct. 2016.

[35] D. Slomovitz, "Electronic system for increasing the accuracy of in-service instrument-current transformers," *IEEE Trans. Instrum. Meas.*, vol. 52, no. 2, pp. 408–410, Apr. 2003.

Qili Zhao (Member, IEEE) received the Ph.D. degree in control theory and control engineering from Nankai University, Tianjin, China, in 2014.

He was a Post-Doctoral Researcher with the Robotics and Mechatronics Research Laboratory, Department of Mechanical and Aerospace Engineering, Monash University, Melbourne, VIC, Australia, from 2014 to 2015, and a Post-Doctoral Fellow with the Advanced Micro and Nanosystems Laboratory, Department of Mechanical and Industrial Engineering, Toronto University, Toronto, ON, Canada, from 2015 to 2018. He is currently an Associate Professor with the College of Artificial Intelligence, Nankai University. His current research interests include robotic patch clamp, robotic cell manipulation, and robotic cell measurement.

Jinyu Qiu (Graduate Student Member, IEEE) received the B.Eng. degree in automation from the Taiyuan University of Technology, Taiyuan, China, in 2019. He is currently pursuing the Ph.D. degree with the College of Artificial Intelligence, Nankai University, Tianjin, China.

His current research interests include robotic patch clamp system, micromanipulators, and microsystems.

Yu Han received the master's degree in control science and engineering from Nankai University, Tianjin, China, in 2021.

He is currently with the Agricultural Bank of China, Tianjin, where he is involved in research and development. His research area is key technology for robotic patch clamp.

Yiqing Jia received the B.Eng. degree in intelligent science and technology and the M.Eng. degree in control science and engineering from Nankai University, Tianjin, China, in 2018 and 2021, respectively. Her current research interests include automated patch clamp robot and biology pattern simulation.

Yue Du (Member, IEEE)received the Ph.D. degree from the National University of Singapore, Singapore, in 2015.

She pursued a post-doctoral study with the University of Oklahoma, Norman, OK, USA. She is currently a Lecturer with the Artificial Intelligence College, Nankai University, Tianjin, China. She has carried out in-depth research in the intersection of engineering, biology, and medicine, such as micromanipulation robot systems, smart medicine, and biophysical analysis.

Huiying Gong is currently pursuing the Ph.D. degree with the College of Artificial Intelligence, Nankai University, Tianjin, China.

Her current research interests include micromanipulators and microscope image processing.

Minghui Li received the bachelor's degree in mechanical engineering from Beijing Jiaotong University, Beijing, China, in 2021. She is currently pursuing the master's degree in control science and engineering with Nankai University, Tianjin, China.

Her current research interests include micromanipulators and microsystems.

Ruimin Li is currently pursuing the bachelor's degree with the School of Intelligence Science and Technology, Hebei University of Technology, Tianjin, China.

She will begin the Ph.D. degree studies with Nankai University, Tianjin, in 2022. Her current research interests include micromanipulators and microsystems.

Mingzhu Sun (Member, IEEE) received the B.S., M.S., and Ph.D. degrees in computer science and technology, computer application, control theory, and control engineering from Nankai University, Tianjin, China, in 2003, 2006, and 2009, respectively.

Since 2009, she has been with the Institute of Robotics and Automatic Information System and the Department of Automation and Intelligence Science, Nankai University. She is currently an Associate Professor of micromanipulation. Her current research interests include micromanipulator for life science, image processing, and computer vision.

Xin Zhao (Member, IEEE) received the B.S. degree in control theory and control engineering from Nankai University, Tianjin, China, in 1991, the M.S. degree in control theory and control engineering from the Shenyang Institute of Automation, CAS, Shenyang, China, in 1994, and the Ph.D. degree in control theory and control engineering degree from Nankai University in 1997.

He joined the faculty at Nankai University in 1997, where he is currently a Professor and the Dean of the College of Artificial Intelligence. His current research interests include micromanipulator, microsystems, and mathematical biology.